

# Proving Optical Anisotropy and Polarization Effects in $\beta$ -Ga<sub>2</sub>O<sub>3</sub> Nanomembranes via X-Ray Excited Optical Luminescence

Paula Pérez-Peinado, Jaime Dolado,\* Pedro L. Alcázar Ruano, Daniel Carrasco, Ruth Martínez-Casado, Valentina Bonino, Gema Martínez-Criado, Jani Jesenovec, John S. McCloy, Francisco Domínguez-Adame, Jorge Quereda, Emilio Nogales, and Bianchi Méndez\*

Monoclinic  $\beta$ -Ga<sub>2</sub>O<sub>3</sub> is a key representative material of the ultrawide-bandgap semiconductor family. The distinct atomic arrangement in  $\beta$ -Ga<sub>2</sub>O<sub>3</sub> introduces two coordination environments for Ga ions, resulting in pronounced anisotropy in its optical, electronic, and thermal properties. In this study, a synchrotron nanoprobe to investigate the anisotropic optical properties of well-oriented (100)  $\beta$ -Ga<sub>2</sub>O<sub>3</sub> nanomembranes with a thickness of 200 nm, produced through mechanical exfoliation, is employed. Polarization-resolved X-ray excited optical luminescence (XEOL) measurements reveal a strong ultraviolet (UV) emission band at 3.4 eV, which is strongly polarized along the *c*-axis. Additionally, XEOL data show blue (2.9 eV) and deep-UV (3.8 eV) emissions. Notably, the deep-UV band, rarely reported in conventional photoluminescence studies, is attributed to the presence of Ga vacancies, as supported by first-principles calculations. Polarization-dependent X-ray absorption near-edge structure (XANES) spectroscopy allows one to probe the distinct symmetries of the *b* and *c* crystallographic planes. Furthermore, by combining XANES and XEOL, this study investigates the site-specific contributions of Ga ions to the luminescence process. These findings highlight the potential of  $\beta$ -Ga<sub>2</sub>O<sub>3</sub> nanomembranes as a robust material platform for developing polarization-sensitive devices. The pronounced anisotropy of  $\beta$ -Ga<sub>2</sub>O<sub>3</sub> causes orientation-dependent optoelectronic properties, making it a highly promising candidate for a wide range of advanced applications.

## 1. Introduction

Ga<sub>2</sub>O<sub>3</sub> is the main representative semiconductor in the ultrawide-bandgap materials family, with significant potential in high-power electronic devices, high-frequency telecommunications, solar blind ultraviolet (UV) photodetectors, or tunable light emitters, often surpassing GaN or SiC performance in these applications.<sup>[1–3]</sup> Among its five known polymorphs, the monoclinic  $\beta$ -Ga<sub>2</sub>O<sub>3</sub> phase is the most stable one, exhibiting an indirect electronic bandgap at 4.5 eV, but with direct  $\Gamma - \Gamma$  transitions in the 4.5 – 4.9 eV range that dominate the optical absorption spectrum.<sup>[4]</sup> The atomic arrangement in  $\beta$ -Ga<sub>2</sub>O<sub>3</sub> distinguishes two symmetries for Ga ions, labeled as Ga<sub>I</sub> and Ga<sub>II</sub>, with tetrahedral and octahedral coordination, respectively. The GaO<sub>4</sub> tetrahedra and GaO<sub>6</sub> octahedra are aligned with the *b* direction of the monoclinic structure, making this oxide highly anisotropic regarding its optical, electronic, and thermal properties parallel or perpendicular to the *b* direction.<sup>[5,6]</sup> This anisotropy gives rise to several

P. Pérez-Peinado, P. L. Alcázar Ruano, D. Carrasco, R. Martínez-Casado, F. Domínguez-Adame, E. Nogales, B. Méndez  
Departamento Física de Materiales  
Universidad Complutense de Madrid  
28040 Madrid, Spain  
E-mail: bianchi@ucm.es

J. Dolado, V. Bonino, G. Martínez-Criado  
European Synchrotron Radiation Facility  
ESRF  
Grenoble 38043, France  
E-mail: doladofe@esrf.fr

G. Martínez-Criado, J. Quereda  
Instituto de Ciencia de Materiales de Madrid (ICMM-CSIC)  
E-28049 Madrid, Spain

G. Martínez-Criado, J. Quereda  
2D Foundry Group (ICMM-CSIC)  
E-28049 Madrid, Spain

J. Jesenovec, J. S. McCloy  
Institute of Materials Research  
Washington State University  
Pullman 99163, USA

 The ORCID identification number(s) for the author(s) of this article can be found under <https://doi.org/10.1002/adpr.202500043>.

© 2025 The Author(s). Advanced Photonics Research published by Wiley-VCH GmbH. This is an open access article under the terms of the Creative Commons Attribution License, which permits use, distribution and reproduction in any medium, provided the original work is properly cited.

DOI: 10.1002/adpr.202500043

distinctive optical phenomena, including birefringence and dichroism;<sup>[7,8]</sup> a refractive index that exhibits a strong dependence on the crystallographic direction;<sup>[9]</sup> and a polarization-dependent optical absorption edge. The latter arises from the selection rules governing dipole-allowed transitions between conduction and valence band states, resulting in absorption edge values ranging from 4.54 eV when the electric field  $E$  is aligned parallel to the  $c$  axis, to 4.90 eV for  $E$  parallel to the  $b$  axis.<sup>[10]</sup>

To fully exploit the unique optical properties of  $\beta$ -Ga<sub>2</sub>O<sub>3</sub>, a thorough understanding of its luminescence mechanisms is essential. To date, the luminescence of  $\beta$ -Ga<sub>2</sub>O<sub>3</sub> has mainly been investigated using photoluminescence (PL)<sup>[11,12]</sup> and cathodoluminescence (CL).<sup>[13,14]</sup> In unintentionally doped  $\beta$ -Ga<sub>2</sub>O<sub>3</sub>, the luminescence primarily features a broad UV emission band (3.1–3.4 eV) caused by the recombination of free electrons with self-trapped holes (STHs), which suppresses near-band-edge emission.<sup>[15,16]</sup> In addition to this UV emission, radiative recombination from donor–acceptor pairs (DAP) has been claimed as responsible for emission bands in the blue (2.58–3.02 eV) and green (2.07–2.48 eV) range. Donors are often attributed to oxygen vacancies ( $V_{\text{O}}$ ) and unintentional impurities like Si. It should be mentioned that the role of oxygen vacancies in the origin of blue emission, composed of several components, is still a controversial issue (see, e.g., ref. [17]). On the other hand, Ga vacancies ( $V_{\text{Ga}}$ ), isolated or forming complexes with  $V_{\text{O}}$ , and Ga interstitials have been suggested as acceptor levels.<sup>[11,12,14]</sup> The characteristics of DAP emissions are highly dependent on defect microstructure, dopant impurities, and synthesis conditions, leading them to be considered extrinsic rather than intrinsic to the material.

The inherent anisotropy of  $\beta$ -Ga<sub>2</sub>O<sub>3</sub> results in polarization-dependent optical responses, positioning it as a promising material for orientation-sensitive applications in photonics and optoelectronics. Polarized PL studies have revealed a strong polarization dependence of the UV emission, with light predominantly polarized along the  $c$  axis, irrespective of the excitation polarization state. However, the spectral shape remains unchanged, suggesting consistent recombination pathways across different crystal orientations.<sup>[10,18]</sup> On the other hand, polarization-sensitive photodetectors based on  $\beta$ -Ga<sub>2</sub>O<sub>3</sub>, exploiting the anisotropy between  $b$  and  $c$  axes in the crystal have also been reported.<sup>[19,20]</sup> Moreover, recent advancements in polarization-sensitive nanowire-based devices with memory consolidation capabilities have expanded the potential of  $\beta$ -Ga<sub>2</sub>O<sub>3</sub> for applications such as image recognition and data encryption.<sup>[21]</sup>

A promising strategy to further tailor the anisotropic optical properties of  $\beta$ -Ga<sub>2</sub>O<sub>3</sub> is through precise control over its architecture and morphology. Nanowires, for instance, exhibit preferred light propagation along their axis and can function as Fabry–Perot optical microcavities with appropriate design.<sup>[22–24]</sup> Many oxides, as MoO<sub>3</sub>, exhibit a layered structure and can be easily exfoliated, leading to flakes.<sup>[25]</sup> On the other hand, nanomembranes (NMs) of nonlayered oxides are also achievable for particular surface orientations for which the interplane bonding energy is low, as is the case for (100) oriented  $\beta$ -Ga<sub>2</sub>O<sub>3</sub> crystals. The successful mechanical exfoliation of ultrathin, free-standing  $\beta$ -Ga<sub>2</sub>O<sub>3</sub> membranes from (100)-oriented crystals opens new avenues for the development of flexible, lightweight, and high-performance optoelectronic devices.

In this work we investigate the anisotropic optical properties of  $\beta$ -Ga<sub>2</sub>O<sub>3</sub> NMs, fabricated via mechanical exfoliation, using polarization-resolved X-ray excited optical luminescence (XEOL). Unlike conventional UV–visible PL, XEOL enables the monitoring of optical luminescence excited by a precisely selected X-ray photon energy. This approach allows for the excitation of specific core levels of elements of interest, promoting transitions to bound, quasibound, and continuum states, thus providing both elemental and, in certain cases, site-specific insights. The absorbed X-ray energy is partially transferred to optical de-excitation channels, resulting in characteristic luminescence emission. Furthermore, by incorporating a polarizer in the detection system, we can analyze the polarization state of the emitted light, which is crucial for the study of polarization-sensitive optoelectronic properties.

On the other hand, X-ray absorption near-edge structure (XANES) spectroscopy probes the modulation of the X-ray absorption coefficient in the near-edge region of a specific core level within the material. By utilizing a tunable synchrotron light source to excite core electrons of an element within its chemical environment, XANES provides valuable insights into the local symmetry and electronic structure of unoccupied states, which are dictated by the surrounding atomic arrangement and bonding characteristics. Traditionally, XANES spectra are acquired via transmission or X-ray fluorescence yield (FLY) methods. However, XEOL can also serve as a detection mode, enabling the photoluminescence yield (PLY) to be tracked across an absorption edge. Under favorable conditions, this approach offers site-specific luminescence information with high sensitivity to local chemical environments. Herein, we aim to unravel the potential influence of the distinct Ga coordination environments in  $\beta$ -Ga<sub>2</sub>O<sub>3</sub> ( $\text{Ga}_{\text{I}}$  and  $\text{Ga}_{\text{II}}$ ) on the observed optical luminescence properties by combining XEOL and XANES measurements. To achieve this, we leveraged the unique capabilities of the ID16B beamline at the European Synchrotron Research Facility (ESRF), which offers state-of-the-art multimodal nanoscale analysis tools.<sup>[26]</sup>

## 2. Results and Discussion

### 2.1. Structural Characterization

The investigated  $\beta$ -Ga<sub>2</sub>O<sub>3</sub> NMs have been produced by mechanical exfoliation of the (100) surface of a Czochralski single crystal with the aid of PVC tape and further transferred to a Si wafer coated by a SiO<sub>2</sub> layer of 285 nm thickness, as shown in **Figure 1a**. This procedure allows us to achieve rectangular-shaped NMs with well-defined edges of several microns width and tens of microns length. The iteration of the process yields thinner membranes until a final critical thickness of the order of tens of nanometers, below which the material becomes unstable.

The thickness of the  $\beta$ -Ga<sub>2</sub>O<sub>3</sub> NMs has been estimated by optical interferometry and atomic force microscopy (AFM) measurements. In the first case, the interference pattern of the reflectance spectrum is fitted for the Ga<sub>2</sub>O<sub>3</sub> (204 nm)/SiO<sub>2</sub> (285 nm)/Si stacking by the transfer matrix method. **Figure 1b** shows the observed optical contrast (blue line) of a Ga<sub>2</sub>O<sub>3</sub> NM, whose

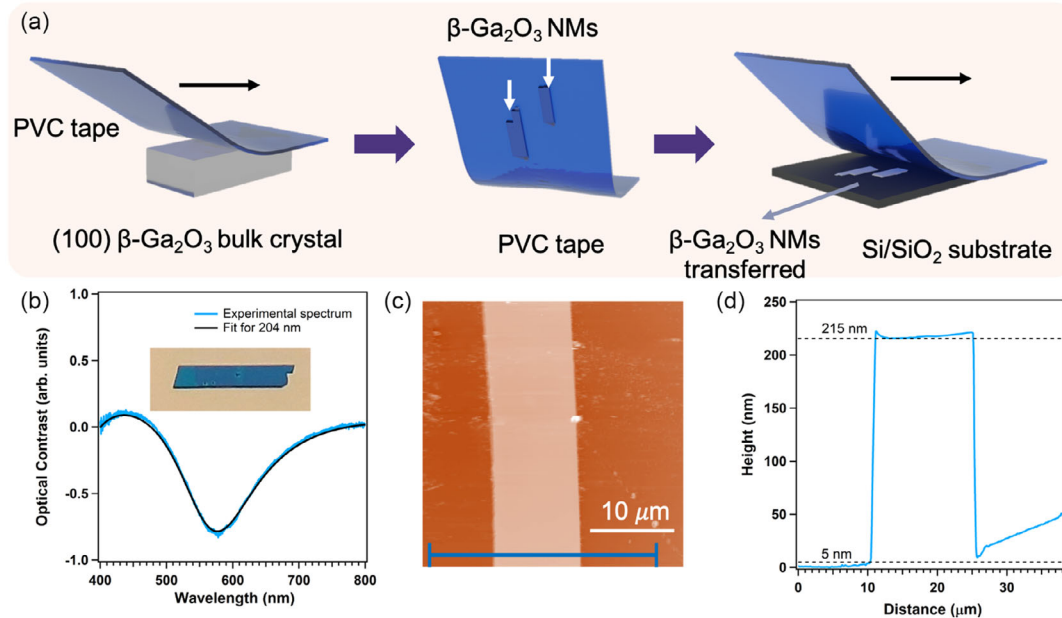


**Figure 1.** a) Sketch of the fabrication sequence of the  $\beta$ -Ga<sub>2</sub>O<sub>3</sub> NMs. b) Experimental data and simulated data of optical contrast fitted to NM thickness of 204 nm. The inset shows an optical image of the NM. c) AFM image of the NM in tapping mode. d) Line profile taken from the AFM image to estimate the thickness of the NM. The result agrees with the value obtained by optical interferometry displayed in (b).

image is shown in the inset, and the calculated one (black line) for a Ga<sub>2</sub>O<sub>3</sub> NM of 204 nm thickness. On the other hand, the surface flatness and height of the NMs have also been assessed by AFM. Figure 1c shows the topographic AFM image of the Ga<sub>2</sub>O<sub>3</sub> NM of 15  $\mu$ m width, and Figure 1d depicts the line profile along the blue line in Figure 1c. A thickness of 210 nm is measured from the plot, in close agreement with the calculated thickness of the Ga<sub>2</sub>O<sub>3</sub> NM derived from the optical contrast image.

The crystallographic directions in these NMs with well-defined morphology can be identified from polarized Raman measurements under specific geometric arrangements, as reported elsewhere.<sup>[27,28]</sup> Figure 2a shows the spatial configuration used to record Raman spectra polarized parallel or perpendicular to the longer edge of a NM. According to Porto's notation, the left side configuration will result in  $-Z(YY)Z$  Raman spectra and the right side in  $-Z(XX)Z$  one. Purple arrows indicate the polarization of the incident laser, while pink or blue arrows stand for the polarization of the Raman signal. Figure 2b shows the polarized Raman spectra parallel (blue line) or perpendicular (pink line) to the longer edge of the NM. The main peaks are identified as the characteristic Raman modes observed in  $\beta$ -Ga<sub>2</sub>O<sub>3</sub>.<sup>[29,30]</sup> It can be clearly observed that some modes are quenched in one configuration or the other. In particular, the  $A_g^{(7)}$  and  $A_g^{(10)}$  modes present maxima in  $-Z(YY)Z$  and  $-Z(XX)Z$ , respectively. The results for multiple polarization angles are shown in Figure 2c for the  $A_g^{(7)}$ ,  $A_g^{(9)}$ , and  $A_g^{(10)}$  modes. These results match with the angle-resolved Raman spectra in  $\beta$ -Ga<sub>2</sub>O<sub>3</sub> crystals with (100) surface, being [010] direction parallel and [001] direction perpendicular to the longer side of the NM.<sup>[30]</sup>

For the sake of clarity, from now on, we will label the orientations according to the crystalline structure within the  $\beta$ -Ga<sub>2</sub>O<sub>3</sub>,

as sketched in Figure 2c. In all produced rectangular NMs, the long edge aligns to the [010] direction and the shorter one to the [001] direction.

## 2.2. XEOL: Polarized Emission

To achieve a deeper understanding of the luminescence properties of  $\beta$ -Ga<sub>2</sub>O<sub>3</sub>, we performed polarization-resolved XEOL measurements on our well-oriented NMs, as illustrated in Figure 3 (for further details on the XEOL setup, refer to the Experimental section). Figure 3a presents the unpolarized XEOL spectrum, revealing the characteristic complex blue-UV emission band of  $\beta$ -Ga<sub>2</sub>O<sub>3</sub>, which has been previously observed in both XEOL and CL studies.<sup>[13,31]</sup> The polarization-resolved XEOL spectra, measured with the polarizer aligned approximately parallel to the *c* and *b* axes, are displayed in Figure 3b,c, respectively. In both polarization configurations, the spectra are well-fitted by three Gaussian components: a deep-UV (D-UV) emission centered at 3.8 eV, a UV emission at 3.4 eV, and a broad blue emission at 2.9 eV.

Significant spectral changes are observed depending on the polarizer orientation. When the emission is collected with the polarizer aligned parallel to the *c*-axis, the UV emission at 3.4 eV dominates over the D-UV and blue components. However, when the polarizer is aligned parallel to the *b*-axis, the 3.4 eV UV emission is significantly quenched, while the D-UV and blue emissions remain relatively unchanged in intensity. This result is reproducible in NMs with thickness in the range of 200–500 nm, although thicker membranes show additional features in the spectra related to interferometric effects that obscure the interpretation of luminescence bands in the

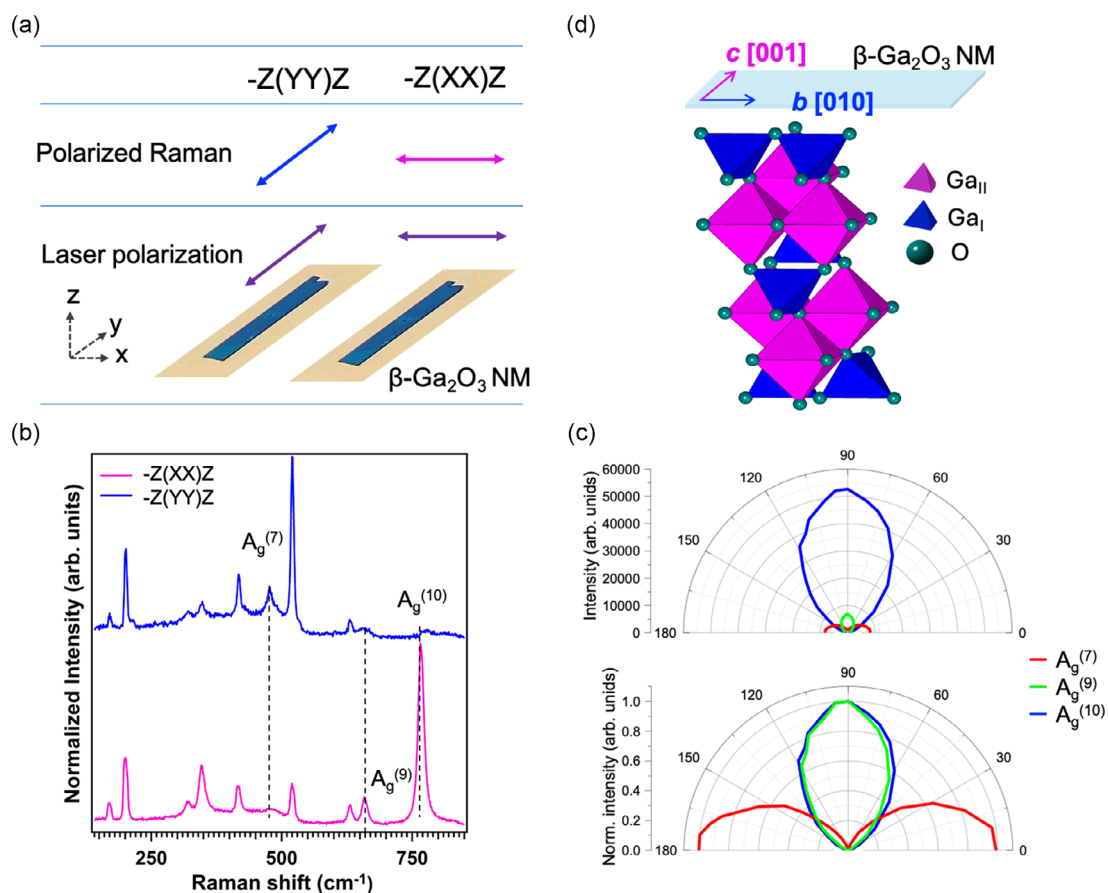


**Figure 2.** a) Sketch of the geometry of the Raman measurements to identify the polarization directions of the incident laser beam and the Raman signal in the laboratory reference frame. Porto's notation is used according to the directions shown in the sketch. b) Polarized Raman spectra for the two configurations displayed in (a). For the sake of clarity, the blue spectrum is vertically shifted. c) Top: Polarogram of intensities of Raman peaks  $A_g^{(7)}$ ,  $A_g^{(9)}$ , and  $A_g^{(10)}$  derived from the Raman spectra taken under angles in the range (0–180) between the polarizer and the long edge of the membrane. Bottom: polarogram with normalized intensities. d) Crystalline structure of  $\beta$ - $\text{Ga}_2\text{O}_3$  and the crystallographic directions in the NM.

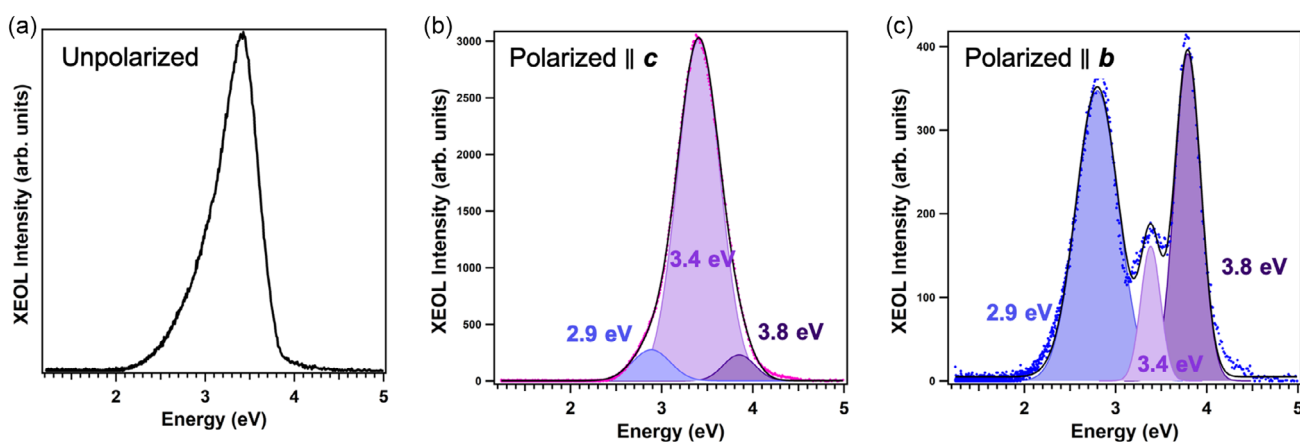


**Figure 3.** a) Unpolarized XEOL spectrum of the NM. XEOL spectra collected with the polarizer oriented b) parallel to the  $c$ -axis and c) parallel to the  $b$ -axis.

range of 300–500 nm. These observations lead us to conclude that the UV emission at 3.4 eV is strongly polarized along the  $c$ -axis, whereas the D-UV and blue emissions exhibit little to

no polarization dependence. These findings are in agreement with previous PL studies, which reported that the intensity of emitted light along the  $b$ -axis is weaker compared to the  $a$  and  $c$  axes.<sup>[10,18]</sup>

### 2.3. Role $V_{Ga}$ : First-Principles Calculations

Let us now discuss the luminescence bands observed in the XEOL spectra. As previously mentioned, the UV emission band at 3.4 eV has been extensively investigated in the literature, with a broad consensus attributing its origin to the recombination of free electrons with STHs localized near the valence band. This emission is widely regarded as an intrinsic property of  $\beta\text{-Ga}_2\text{O}_3$ , as it occurs independently of native defects and is primarily governed by the fundamental electronic structure of the material.<sup>[15,16]</sup>

The origin of the blue emission band, however, remains somewhat ambiguous. It is commonly attributed to DAP recombination, with  $V_O$  acting as donors and  $V_{Ga}$  or  $V_{Ga}\text{-}V_O$  complexes serving as acceptors in unintentionally doped material.<sup>[11,14]</sup> This emission band is typically broad, which is primarily attributed to strong electron-phonon coupling effects, leading to significant spectral broadening and energy dispersion.<sup>[12]</sup>

A particularly intriguing aspect of our results is the observation of the D-UV band in the XEOL spectra, which has been rarely reported in previous PL or CL studies of undoped  $\text{Ga}_2\text{O}_3$ . Although this band is relatively weak, being nearly imperceptible in the unpolarized spectrum, it becomes clearly distinguishable when the dominant UV emission at 3.4 eV is quenched. The presence of this band suggests the involvement of additional electronic states that enable this rarely observed recombination process. Bordun et al. have reported prominent UV/blue emissions at 2.95 and 3.14 eV, along with a weaker D-UV emission in the 3.9–4.2 eV range in  $\beta\text{-Ga}_2\text{O}_3$  thin films synthesized via sputtering.<sup>[32]</sup> They attributed the weak D-UV emission to the recombination of excitons within quantum wells formed by acceptor clusters. This interpretation aligns with a previous model suggested to explain a distinctive structure observed at the optical absorption edge of  $\beta\text{-Ga}_2\text{O}_3$  under unpolarized light, which has been attributed to the formation of low-dimensional acceptor clusters.<sup>[33]</sup> More recently, a 3.8 eV emission has been reported in PL measurements in  $\alpha\text{-Ga}_2\text{O}_3$  and attributed to DAP transition, in which H-related shallow donor and H-decorated  $V_{Ga}$  as the acceptor are involved.<sup>[34]</sup> Finally, investigations into the electrical properties of undoped  $\text{Ga}_2\text{O}_3$  have identified several deep electron traps within the bandgap,

which significantly influence the free carrier concentration and electrical conductivity. Specifically, deep levels located at  $-2.04$ ,  $-2.71$ , and  $-4.30$  eV below the conduction band edge have been associated with native  $V_{Ga}$  and/or compensating impurities in a general way.<sup>[35]</sup>

Thus, it appears that  $V_{Ga}$  plays a significant role in the luminescence of  $\beta\text{-Ga}_2\text{O}_3$ . To further elucidate their contribution to the observed luminescence bands, we performed density functional theory (DFT) calculations to analyze the electronic states associated with  $V_{Ga}$  at both  $\text{Ga}_I$  and  $\text{Ga}_{II}$  sites (see **Figure 4**). The computed density of states reveals the presence of acceptor levels at 0.36 eV above the valence band edge for  $V_{Ga_I}$ , and at 0.10, 0.22, and 0.43 eV above the valence band edge for  $V_{Ga_{II}}$ . These energy levels are in good agreement with previously reported electronic traps identified in studies of the electronic properties of  $\beta\text{-Ga}_2\text{O}_3$ ,<sup>[35]</sup> further supporting the hypothesis that both the D-UV and blue emission bands could potentially be associated with the presence of native  $V_{Ga}$  defects. The relatively weak intensity of these defect-related emissions serves as a strong indicator of the high crystalline quality of the NMs, suggesting a low concentration of native defects, particularly  $V_{Ga}$ .

### 2.4. XANES–XEOL Study: Site-Specific Luminescence Information

Linearly polarized XANES spectroscopy is a powerful technique for probing the electronic structure of specific elements along different crystallographic directions, as, for example, along radial and axial directions in nanowires.<sup>[36]</sup> It provides information about orbital orientation and their contributions to the electronic band states. Recently, Hegde et al. investigated the anisotropic electronic properties of  $\beta\text{-Ga}_2\text{O}_3$  nanowires using linearly polarized XANES at the Ga  $L_3$  and O  $K$ -edges.<sup>[37]</sup> Their study revealed valuable information on the contributions of oxygen atoms to the pronounced linear dichroism observed along the  $b$ -axis, attributing it to the hybridization between O  $2p$  and Ga  $4p$  orbitals. Specifically, they analyzed the role of O  $2p_{x,y}$  and O  $2p_z$  orbitals in shaping the valence band structure.

Here, leveraging the linear polarization of the X-ray beam, Ga  $K$ -edge XANES spectra were recorded along the NMs. When the electric field of the incident photons is perpendicular to the  $c$ -axis

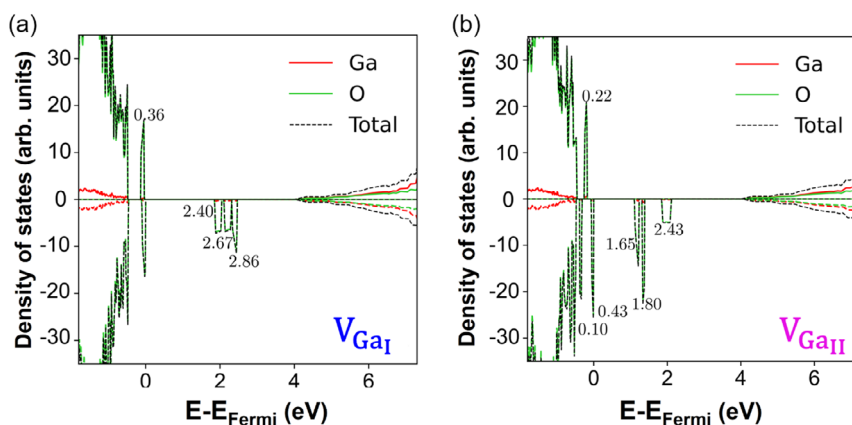


**Figure 4.** Density of states of  $\beta\text{-Ga}_2\text{O}_3$  with a)  $V_{\text{Ga}_I}$  and b)  $V_{\text{Ga}_{II}}$  vacancies. The energy of electronic states within the bandgap is indicated.

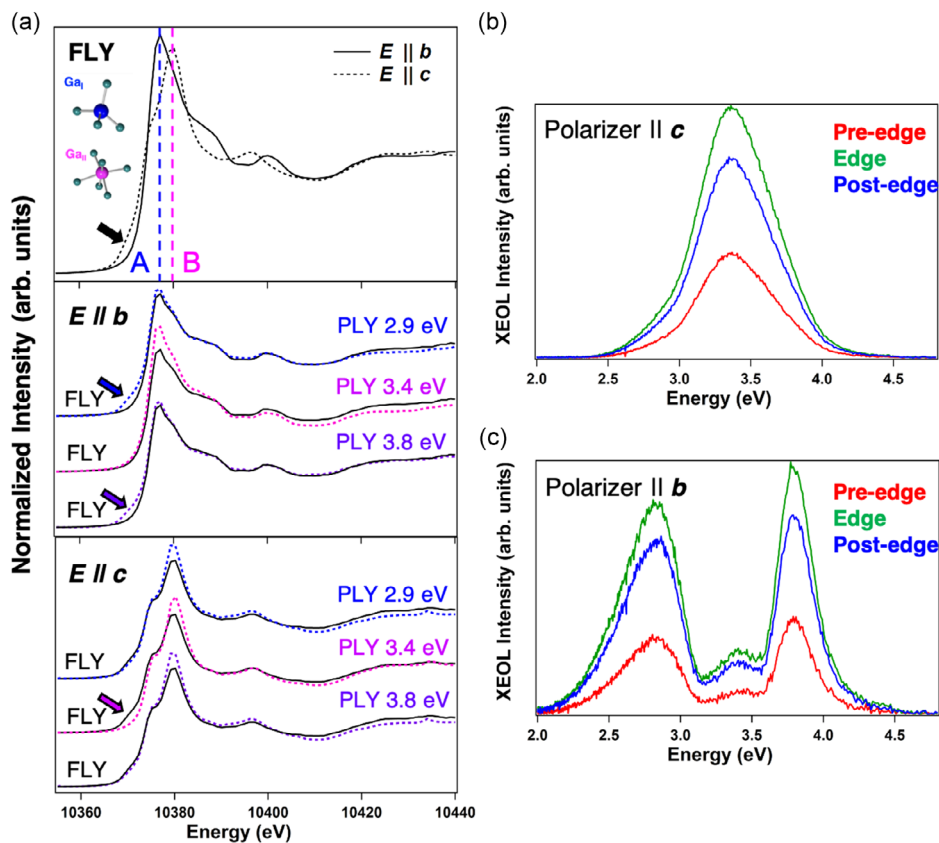
( $E \parallel b$ ), transitions from the Ga 1s core level to the  $4p_y$  conduction band states are allowed, thus probing the symmetry of the (001) plane. Conversely, when the  $c$ -axis of the NM is aligned parallel to the electric field vector of the X-ray beam ( $E \parallel c$ ), the XANES measurements provide information on the symmetry of the (010) plane by probing the  $P_z$  conduction band states.<sup>[36]</sup>

Figure 5a (top section) presents the XANES spectra recorded in FLY mode with the electric field of the incident X-ray photons aligned parallel to the  $b$ -axis ( $E \parallel b$ , solid line) and  $c$ -axis ( $E \parallel c$ , dashed line). In both configurations, the spectra exhibit two distinct peaks, labeled A and B, located at  $10.377 \pm 1$  and  $10.380 \pm 1$  eV, respectively. This complex white line arises from the coexistence of  $Ga^{+3}$  ions in  $GaO_4$  tetrahedral and  $GaO_6$  octahedral units. The relative intensity of these peaks serves as a reliable fingerprint for identifying different  $Ga_2O_3$  polymorphs, owing to the distinct symmetries associated with each phase.<sup>[38,39]</sup> Specifically, the lower-energy peak corresponds to Ga atoms in tetrahedral coordination ( $Ga_I$ ), while the higher-energy peak is attributed to Ga atoms in octahedral coordination ( $Ga_{II}$ ).<sup>[40]</sup>

Our results demonstrate a clear polarization dependence: X-rays polarized along the  $b$ -axis are predominantly absorbed by  $Ga_I$  sites (at 10.377 eV), whereas X-rays polarized along the  $c$ -axis

primarily interact with  $Ga_{II}$  sites (at 10.380 eV). This observation indicates a variation in the relative distribution of Ga coordination environments between the (001) and (010) planes, consistent with the monoclinic crystalline structure of  $\beta$ - $Ga_2O_3$ . In the (001) planes, the density of tetrahedral and octahedral sites is equal, while in the (010) planes, octahedral sites dominate. The observed variation in white line intensity arises from the greater covalent character of  $Ga_I$  compared to  $Ga_{II}$ , due to its lower coordination number, which enhances hybridization with surrounding oxygen atoms.<sup>[37]</sup> By simply rotating the  $\beta$ - $Ga_2O_3$  NM relative to the X-ray electric field, the absorption response of Ga ions can be selectively tuned. This provides a valuable tool for investigating physical properties related to orbital symmetries, bond character (e.g., covalency), and orbital contributions to electronic band states, all of which are directly linked to the pronounced anisotropic behavior observed in  $\beta$ - $Ga_2O_3$ .

When combined with XANES, XEOL serves as a powerful tool to uncover the origin of luminescence and the underlying mechanisms of energy transfer to the optical channel responsible for light emission. To gain deeper insight into how the distinct Ga sites influence these processes, we performed XANES measurements in PLY mode, tracking the XEOL signal across the Ga K-edge, which represents the X-ray absorption coefficient of



**Figure 5.** a, top) XANES spectra recorded in FLY mode with the electric field of the incident X-ray beam aligned parallel to the  $b$ -axis (solid line) and  $c$ -axis (dashed line); (a, middle) and (a, bottom) PLY mode for each XEOL emission (dashed colored lines) under each incident configuration, where preferential absorption by  $Ga_I$  or  $Ga_{II}$  occurs. The corresponding FLY mode XANES spectra (solid black lines) are overlaid for direct comparison, with all the spectra vertically shifted for clarity. b,c) XEOL spectra collected with the polarizer oriented parallel to the  $c$ -axis and  $b$ -axis, respectively, while exciting the sample with different photon energies: below the absorption edge (10.365 eV, red lines), near the absorption edge (10.380 eV, green lines), and above the edge (10.400 eV, blue lines).

the different Ga atoms that contribute to the luminescence. Figure 5a (middle and bottom sections) presents the XANES spectra obtained in both FLY (solid black lines) and PLY (dashed colored lines) modes, with the incident X-ray electric field aligned parallel to the *b*- or *c*-axis, respectively. To independently track the different emission bands, we selected specific spectral regions of interest for each emission. In addition, the UV band (3.4 eV) was monitored with the polarizer aligned parallel to the *c*-axis, while the D-UV and blue bands were tracked with the polarizer aligned parallel to the *b*-axis. This configuration minimizes the contribution of the intense UV band, which could otherwise obscure the weaker D-UV and blue emissions. Our observations reveal that, in all cases, the XANES spectra acquired in PLY mode closely follow the same profile as those recorded in FLY mode beyond the absorption edge. This result has a straightforward interpretation: the XEOL signal is directly proportional to the X-ray absorption coefficient. In other words, the light emitted by the material is proportional to the absorption of incident X-ray photons by the Ga atoms.

The mechanisms governing XEOL are inherently complex, involving an energy transfer process initiated by the decay of a core hole, followed by a cascade of subsequent relaxation events. On one hand, the measurement configuration plays a crucial role, as the use of hard or soft X-rays affects both the absorption cross-section and the thermalization pathway of secondary excitation processes. On the other hand, the XEOL signal is highly dependent on the material under study, as these energy transfer processes are influenced by factors such as composition, structure, morphology, crystallinity, defect concentration, and overall material quality. From our results, we observe that the XANES profiles monitored in PLY mode exhibit the same spectral shape as those obtained in FLY mode, depending on whether the electric field vector of the X-ray beam is aligned parallel to the *b* or *c* axes. Therefore, although the spectral features of the XEOL signal remain unchanged regardless of the incident polarization, the intensity variation along the Ga *K*-edge reflects whether the photons are absorbed by Ga<sub>I</sub> or Ga<sub>II</sub> sites. The fact that the XANES spectra in PLY mode closely follow the FLY mode profiles, depending on whether Ga<sub>I</sub> or Ga<sub>II</sub> sites are excited, indicates that the absorption by both types of Ga ions contributes to the luminescence process. In other words, the luminescence (a secondary process) follows the probability of the primary absorption mechanism.

Figure 5b,c present the XEOL spectra collected with the polarizer aligned parallel to the *c*-axis and *b*-axis, respectively, while exciting the sample with different photon energies: below the absorption edge (10.365 eV, red curves), near the absorption edge (10.380 eV, green curves), and above the edge (10.400 eV, blue curves). Notably, the overall shape of the XEOL emission remains identical regardless of the excitation energy in each case, with variations observed only in intensity. This indicates that the Ga ions themselves are not the primary factor dictating the XEOL mechanism, as the luminescence signal persists well below the Ga *K*-edge. Instead, reaching the *K* absorption edge acts as an additional excitation pathway, increasing the number of electrons available for the radiative decay process. This effectively amplifies the luminescence intensity without altering the intrinsic recombination dynamics.

A more detailed examination of the spectra reveals distinct differences in white line intensities. When Ga<sub>I</sub> sites are excited ( $E||b$ ), the XANES spectra in PLY mode for the UV emission (3.4 eV) exhibit a more intense white line compared to FLY mode. In contrast, the XANES spectra in PLY mode for the blue (2.9 eV) and deep-UV (3.8 eV) emissions closely resemble the corresponding FLY spectra. This suggests a higher luminescence efficiency for the UV emission when exciting Ga<sub>I</sub> near the absorption edge. This effect may arise from a more efficient charge transfer to the luminescence channel responsible for the UV band or from a stronger chemical association between Ga<sub>I</sub> sites and the UV emission process. When Ga<sub>II</sub> sites are excited ( $E||c$ ), all XANES spectra in PLY mode exhibit a slightly more intense white line compared to FLY mode. These observations suggest that site-specific electronic environments influence the luminescence process differently, with Ga<sub>I</sub> sites playing a more significant role in UV emission, while Ga<sub>II</sub> sites contribute more uniformly across all emission bands.

A closer inspection of the PLY XANES results reveals additional anomalies. Figure 5a (middle section) shows that when the Ga<sub>I</sub> sites are excited ( $E||b$ ), the blue (2.9 eV) and D-UV (3.8 eV) bands exhibit a slight shoulder at the onset of the white line, a feature absent in XANES spectra in FLY and PLY for the UV emission (3.4 eV). These discrepancies, highlighted with arrows in Figure 5a, have a strong resemblance to the differences previously observed between the FLY XANES spectra for Ga<sub>I</sub> and Ga<sub>II</sub> sites in Figure 5a (top section). In fact, overlaying the curves demonstrates that the initial part of the XANES in PLY mode for the blue and D-UV bands, when exciting Ga<sub>I</sub> sites, closely matches the XANES in FLY mode for Ga<sub>II</sub> sites (see Figure S1a, Supporting Information). In contrast, Figure 5a (bottom section) presents the opposite behavior when Ga<sub>II</sub> sites are excited ( $E||c$ ). In this case, the XANES spectra in PLY mode for the blue and D-UV bands closely resemble the FLY spectra for Ga<sub>II</sub>. However, the onset of the white line in PLY for the UV band deviates from the FLY spectra for Ga<sub>II</sub> and instead overlaps with the FLY XANES profile of Ga<sub>I</sub> sites (see Figure S1b, Supporting Information).

The discrepancy observed in the initial shape of the white line between PLY and FLY modes may be influenced by factors such as lattice disorder, defects, or inhomogeneities, which can modify electronic relaxation pathways and contribute to the luminescence process. A key aspect to consider here is the potential distortion in the XANES spectra obtained in PLY mode due to the complexity of its normalization. While both FLY and PLY XANES spectra are normalized by the photon flux, the normalization process for PLY is inherently more challenging, as the XEOL signal arises from multiple secondary processes rather than a single fluorescence emission event, as in FLY mode. Nevertheless, despite this potential source of variation, the results remained reproducible. Taking this into account, the fact that the anomalies observed in the XANES spectra obtained in PLY mode for one configuration coincide with the FLY spectrum of the opposite configuration suggests a possible correlation: The UV emission appears to be more associated with Ga<sub>I</sub> sites, while the blue and D-UV emissions are more closely linked to the Ga<sub>II</sub> environment.

These findings could represent a significant advancement in XANES–XEOL studies. Traditionally, the use of this technique to investigate luminescence origins has been predominantly

applied to mixed-phase systems with distinct chemical states.<sup>[41,42]</sup> In such cases, XANES monitoring via wavelength-selected PLY has been effective, as the selected wavelength corresponds to a specific chemical environment, allowing for clear differentiation of emission contributions. In contrast, our study extends the applicability of this approach by demonstrating its effectiveness in a single-phase system,  $\beta$ -Ga<sub>2</sub>O<sub>3</sub>, where distinguishing between Ga sites is far more intricate than in mixed systems such as ZnO–ZnS.<sup>[43]</sup> However, further studies are necessary to fully understand the subtle differences observed between the XANES spectra in FLY and PLY modes for the two distinct Ga sites in  $\beta$ -Ga<sub>2</sub>O<sub>3</sub> NMs.

### 3. Conclusions

Undoped  $\beta$ -Ga<sub>2</sub>O<sub>3</sub> nanomembranes have been successfully fabricated through mechanical exfoliation from (100) Czochochalski-grown single crystals and subsequently transferred onto Si substrates for characterization. Polarized Raman measurements confirm that the rectangular-shaped nanomembranes have their longer edge aligned parallel to the *b*-axis and the shorter edge parallel to the *c*-axis of the unit cell. This orientation is particularly significant in such an anisotropic material, where many physical properties exhibit strong orientation dependence. XEOL measurements revealed three distinct emission components: a blue band at 2.9 eV, a UV band at 3.4 eV, and a deep-UV band at 3.8 eV. Polarization-resolved XEOL studies demonstrated that the UV emission at 3.4 eV is strongly polarized along the *c*-axis, while the D-UV and blue emissions show little to no polarization dependence. The incorporation of a polarizer enabled the clear identification of the D-UV band in the XEOL spectra, a feature that has been rarely reported previously. Although the precise origin of this band remains unclear, first-principles calculations provide support for the hypothesis that it is associated with V<sub>Ga</sub>. XANES measurements in FLY mode allowed us to distinguish the two distinct symmetries associated with Ga in  $\beta$ -Ga<sub>2</sub>O<sub>3</sub>. The spectra revealed two characteristic peaks corresponding to Ga atoms in tetrahedral (Ga<sub>T</sub>) and octahedral (Ga<sub>O</sub>) coordination environments. Finally, XANES measurements performed in PLY mode, tracking the XEOL signal across the Ga *K*-edge, provide evidence of a possible site-specific contribution of Ga atoms to the luminescence process. The results suggest that the UV emission at 3.4 eV is more associated with Ga<sub>T</sub> sites, while the blue and deep-UV emissions appear to be more related to Ga<sub>O</sub> sites. These findings provide new insights into the optical anisotropy and polarization effects in  $\beta$ -Ga<sub>2</sub>O<sub>3</sub>. The well-defined behavior in terms of polarization emission connected to specific Ga sites will indeed widen the capabilities of future devices in terms of probing and sensing. The nanomembranes presented in this work, characterized by their high crystalline quality and well-oriented edges relative to the crystallographic axes, facilitate the exploitation of  $\beta$ -Ga<sub>2</sub>O<sub>3</sub>'s anisotropic properties for advanced optoelectronic devices.

### 4. Experimental Section

**Nanomembranes Fabrication:** The  $\beta$ -Ga<sub>2</sub>O<sub>3</sub> NMs were obtained by mechanical exfoliation of an unintentionally doped bulk  $\beta$ -Ga<sub>2</sub>O<sub>3</sub> crystal

grown by Czochochalski and vertical gradient freeze techniques. The exfoliation process was performed along the (100) crystallographic plane using Nitto SPV224 PVC tape, resulting in NMs with thicknesses in the range of several hundred nanometers. These NMs were subsequently transferred onto Si wafers coated with a silicon oxide layer of 285 nm thickness.

**Characterization Methods:** The thickness of the NMs was measured by optical interferometry and AFM. For optical interferometry, a microreflectance system equipped with a CCD charge-coupled device spectrometer integrated into a Motic optical microscope was employed. AFM measurements were performed using a Nanotec AFM system operating in contact mode. Polarized micro-Raman spectroscopy was conducted using the Horiba LabRAM HR800 optical confocal microscope to determine the crystallographic orientation of the axis and the surface planes of the NMs.

**Synchrotron Measurements:** We conducted the synchrotron measurements at the ID16B nanoanalysis beamline of the ESRF. The monochromatic X-ray beam was focused to a spot size of 80 × 70 nm<sup>2</sup>, with an intensity of ≈10<sup>11</sup> photons per second.

XEOL was detected perpendicular to the sample surface using a far-field optical collection system configured in a backscattering geometry. The setup employed an off-axis parabolic mirror (MPD019-H23-F01-SP-2, UV–VIS) with a central hole, allowing the X-ray beam to pass through and reach the sample while simultaneously collecting the luminescence emitted from the front surface. A secondary mirror (RC12SMA-F01, UV) was used to capture the collimated light from the first mirror and focus it into an optical fiber for analysis. To examine the polarization state of the emitted light, a linear polarizer was placed before the second mirror, specifically designed for the 365–395 nm wavelength range. While collimators of this type may induce a slight phase shift, potentially introducing a small degree of ellipticity to the initially linearly polarized light, the general polarization trend can still be reliably assessed. By setting the polarizer at 0° and 90°, we ensured a consistent investigation of the polarization state of the emitted luminescence.

XANES data were acquired around the Ga *K*-edge (10.370 keV) in both FLY and PLY modes, respectively. For FLY measurements, a Si(111) double-crystal monochromator was employed, whereas the PLY measurements utilized the previously described optical collection system. For linearly polarized XANES measurements, we utilized the linear polarization of the synchrotron X-ray beam. To control the incoming polarization, the *c*-axis of the nanomembranes was aligned either parallel or perpendicular to the electric field vector of the incident radiation, enabling a precise investigation of anisotropic absorption effects.

**Density Functional Theory Calculations:** All DFT calculations were performed using the CRYSTAL program,<sup>[44]</sup> in which the crystalline orbitals were expanded as a linear combination of atom-centered Gaussian orbitals, the basis set. The gallium and oxygen ions were described using all-electron basis sets contracted as s(8)p(64111)d(41) and s(8)p(411)d(1), respectively. The obtained bandgap for bulk  $\beta$ -Ga<sub>2</sub>O<sub>3</sub> was 4.4 eV, which was in agreement with the experimental value and validated the considered model. Integration over the reciprocal space was carried out using Monkhorst–Pack meshes of 6 × 6 × 6. The self-consistent field algorithm was set to converge at the point at which the change in energy was less than Hartree per unit cell. The internal coordinates were determined by minimization of the total energy within an iterative procedure based on the total energy gradient calculated with respect to the nuclear coordinates. Convergence was determined from the root mean square (rms) and the absolute value of the largest component of the forces. The thresholds for the maximum and the rms forces (the maximum and the rms atomic displacements) were set to 0.00045 and 0.00030 (0.00180 and 0.0012) in atomic units. Geometry optimization was halted when all four conditions were satisfied simultaneously. For the calculation of Ga vacancies, a supercell with 80 atoms was considered to avoid the interaction between surrounding defects.

### Supporting Information

Supporting Information is available from the Wiley Online Library or from the author.

## Acknowledgements

The authors acknowledge financial support from Comunidad de Madrid (Recovery, Transformation and Resilience Plan) and NextGenerationEU from the European Union (Grant MAD2D-CM-UCM4/5) and Agencia Estatal de Investigación of Spain (Grants PID2021-122562NB-I00 and PID2022-136285NB-C31/3). The authors also acknowledge the support from the Air Force Office of Scientific Research under Award No. FA8655-20-1-7013 (Program Manager: Ali Sayir). J.D. especially acknowledges the financial support of ESRF for his postdoctoral fellowship position. The authors thank the ESRF for the beamtime granted for this work on the beamline ID16B (experiment: MA-6177).

## Conflict of Interest

The authors declare no conflict of interest.

## Data Availability Statement

The data that support the findings of this study are available from the corresponding author upon reasonable request.

## Keywords

gallium oxide, nanomembranes, polarizations, X-ray absorption, X-ray excited optical luminescence

Received: February 20, 2025

Revised: May 21, 2025

Published online:

- [1] S. J. Pearton, J. Yang, P. H. Cary, F. Ren, J. Kim, M. J. Tadjer, M. A. Mastro, *Appl. Phys. Rev.* **2018**, 5, 011301.
- [2] M. Higashiwaki, G. H. Jessen, *Appl. Phys. Lett.* **2018**, 112, 060401.
- [3] H. Deng, K. J. Leadle, Y. Miao, D. S. Black, K. E. Urbaneck, J. McNeur, M. Kozák, A. Ceballos, P. Hommelhoff, O. Solgaard, R. L. Byer, J. S. Harris, *Adv. Opt. Mater.* **2020**, 8, 1901522.
- [4] J. B. Varley, J. R. Weber, A. Janotti, C. G. Van de Walle, *Appl. Phys. Lett.* **2010**, 97, 142106.
- [5] T. Matsumoto, M. Aoki, A. Kinoshita, T. Aono, *Jpn. J. Appl. Phys.* **1974**, 13, 1578.
- [6] N. Ueda, H. Hosono, R. Waseda, H. Kawazoe, *Appl. Phys. Lett.* **1997**, 70, 3561.
- [7] P. Gopalan, S. Knight, A. Chanana, M. Stokey, P. Ranga, M. A. Scarpulla, S. Krishnamoorthy, V. Darakchieva, Z. Galazka, K. Irmischer, A. Fiedler, S. Blair, M. Schubert, B. Sensale-Rodriguez, *Appl. Phys. Lett.* **2020**, 117, 252103.
- [8] M. M. R. Adnan, D. Verma, C. Sturm, M. Schubert, R. C. Myers, *Phys. Rev. Appl.* **2024**, 21, 054059.
- [9] D. Carrasco, E. Nieto-Pinero, M. Alonso-Orts, R. Serna, J. M. San Juan, M. L. Nó, J. Jesenovc, J. S. McCloy, E. Nogales, B. Méndez, *Nanomaterials* **2023**, 13, 6.
- [10] M. Yamaga, T. Ishikawa, M. Yoshida, T. Hasegawa, E. G. Villora, K. Shimamura, *Phys. Status Solidi C* **2011**, 8, 2621.
- [11] L. Binet, D. Gourier, *J. Phys. Chem. Solids* **1998**, 59, 1241.
- [12] K. Shimamura, E. G. Villora, T. Ujiie, K. Aoki, *Appl. Phys. Lett.* **2008**, 92, 201914.
- [13] E. Nogales, B. Méndez, J. Piqueras, *Appl. Phys. Lett.* **2005**, 86, 113112.
- [14] T. Onuma, S. Fujioka, T. Yamaguchi, M. Higashiwaki, K. Sasaki, T. Masui, T. Honda, *Appl. Phys. Lett.* **2013**, 103, 041910.
- [15] J. B. Varley, A. Janotti, C. Franchini, C. G. Van de Walle, *Phys. Rev. B* **2012**, 85, 081109.
- [16] K. A. Mengle, G. Shi, D. Bayerl, E. Kioupakis, *Appl. Phys. Lett.* **2016**, 109, 212104.
- [17] X. Zhu, Y.-W. Zhang, S.-N. Zhang, X.-Q. Huo, X.-H. Zhang, Z.-Q. Li, *J. Lumin.* **2022**, 246, 118801.
- [18] J. Cooke, M. Lou, M. A. Scarpulla, B. Sensale-Rodriguez, *J. Vac. Sci. Technol. A* **2024**, 42, 022801.
- [19] X. Chen, W. Mu, Y. Xu, B. Fu, Z. Jia, F.-F. Ren, S. Gu, R. Zhang, Y. Zheng, X. Tao, J. Ye, *ACS Appl. Mater. Interfaces* **2019**, 11, 7131.
- [20] Y. Zhang, H. Liang, F. Xing, Q. Gao, Y. Feng, Y. Sun, Z. Mei, *Sci. China-Phys. Mech. Astron.* **2024**, 67, 247312.
- [21] Z. Wang, G. Zhang, X. Zhang, C. Wu, Z. Xia, H. Hu, F. Wu, D. Guo, S. Wang, *Adv. Opt. Mater.* **2024**, 12, 2401256.
- [22] E. Nogales, J. Á. García, B. Méndez, J. Piqueras, *Appl. Phys. Lett.* **2007**, 91, 133108.
- [23] M. Alonso-Orts, E. Nogales, J. M. San Juan, M. L. Nó, J. Piqueras, B. Méndez, *Phys. Rev. Appl.* **2018**, 9, 064004.
- [24] M. Alonso-Orts, G. Chilla, R. Hötzel, E. Nogales, J. M. S. Juan, M. L. Nó, M. Eickhoff, B. Méndez, *Opt. Lett.* **2021**, 46, 278.
- [25] A. Arash, T. Ahmed, A. Govind Rajan, S. Walia, F. Rahman, A. Mazumder, R. Ramanathan, S. Sriram, M. Bhaskaran, E. Mayes, M. S. Strano, S. Balendhran, *2D Materials* **2019**, 6, 035031.
- [26] G. Martínez-Criado, J. Villanova, R. Tucoulou, D. Salomon, J.-P. Suuronen, S. Labouré, C. Guilloud, V. Valls, R. Barrett, E. Gagliardini, Y. Dabin, R. Baker, S. Bohic, C. Cohen, J. Morse, *J. Synchrotron Rad.* **2016**, 23, 344.
- [27] J. Dolado, P. Hidalgo, B. Méndez, *Phys. Status Solidi A* **2018**, 215, 1800270.
- [28] M. Alonso-Orts, D. Carrasco, J. M. San Juan, M. L. Nó, A. de Andrés, E. Nogales, B. Méndez, *Small* **2022**, 18, 2105355.
- [29] D. Dohy, G. Lucazeau, A. Revcolevschi, *J. Solid State Chem.* **1982**, 45, 180.
- [30] C. Kranert, C. Sturm, R. Schmidt-Grund, M. Grundmann, *Sci. Rep.* **2016**, 6, 35964.
- [31] X. T. Zhou, F. Heigl, J. Y. P. Ko, M. W. Murphy, J. G. Zhou, T. Regier, R. I. R. Blyth, T. K. Sham, *Phys. Rev. B* **2007**, 75, 125303.
- [32] O. M. Bordun, B. O. Bordun, I. Y. Kukharsky, I. I. Medvid, *J. Appl. Spectrosc.* **2015**, 84, 46.
- [33] L. Binet, D. Gourier, *Appl. Phys. Lett.* **2000**, 77, 1138.
- [34] D. Nicol, Y. Oshima, J. W. Roberts, L. Penman, D. Cameron, P. R. Chalker, R. W. Martin, F. C.-P. Massabuau, *Appl. Phys. Lett.* **2023**, 122, 062102.
- [35] Y. Nakano, *ECS J. Solid State Sci. Technol.* **2017**, 6, P615.
- [36] J. Segura-Ruiz, G. Martínez-Criado, M. H. Chu, S. Geburt, C. Ronning, *Nano Lett.* **2011**, 11, 5322.
- [37] M. Hegde, I. D. Hosein, P. V. Radovanovic, *J. Phys. Chem. C* **2015**, 119, 17450.
- [38] G. Martínez-Criado, J. Segura-Ruiz, M.-H. Chu, R. Tucoulou, I. López, E. Nogales, B. Mendez, J. Piqueras, *Nano Lett.* **2014**, 14, 5479.
- [39] A. Sharma, M. Varshney, H. Saraswat, S. Chaudhary, J. Parkash, H.-J. Shin, K.-H. Chae, S.-O. Won, *Int. Nano Lett.* **2020**, 10, 71.
- [40] K. Nishi, K.-I. Shimizu, M. Takamatsu, H. Yoshida, A. Satsuma, T. Tanaka, S. Yoshida, T. Hattori, *J. Phys. Chem. B* **1998**, 102, 10190.
- [41] F. Heigl, S. Lam, T. Regier, I. Coulthard, T.-K. Sham, *J. Am. Chem. Soc.* **2006**, 128, 3906.
- [42] M. Murphy, X.-T. Zhou, F. Heigl, T. Regier, T.-K. Sham, in *AIP Conf. Proc.*, American Institute of Physics, College Park, Maryland **2007**, Vol. 882, pp. 764–766.
- [43] M. Murphy, X. Zhou, J. Ko, J. Zhou, F. Heigl, T. Sham, *J. Chem. Phys.* **2009**, 130, 8.
- [44] R. Dovesi, A. Erba, R. Orlando, C. M. Zicovich-Wilson, B. Civalleri, L. Maschio, M. Rérat, S. Casassa, J. Baima, S. Salustro, B. Kirtman, *WIREs Comput. Mol. Sci.* **2018**, 8, e1360.